# 交通部中央氣象局

# 委託研究計畫期末成果報告

## 中大規模地震震源破裂特性近即時分析

計畫類別：□氣象　　□海象　　■地震

計畫編號：MOTC-CWB-107-E-03

執行期間：107 年 1 月 1 日至 107 年 12 月 31 日

計畫主持人：李憲忠

執行機構：中央研究院地球科學研究所

本成果報告包括以下應繳交之附件(或附錄)：

□赴國外出差或研習心得報告 1 份

■赴大陸地區出差或研習心得報告 1 份

□出席國際學術會議心得報告及發表之論文各 1 份

中華民國 107 年 11 月 19 日

# 政府研究計畫期末報告摘要資料表

| 計畫中文名稱 | 中大規模地震震源破裂特性近即時分析 | | |
|---|---|---|---|
| 計畫編號 | MOTC-CWB-107-E-03 | | |
| 主管機關 | 交通部中央氣象局 | | |
| 執行機構 | 中央研究院地球科學研究所 | | |
| 年度 | 107 | 執行期間 | 107/01/01-107/12/31 |
| 本期經費<br>(單位：千元) | 1042.6 | | |
| 執行進度 | 預定（％） | 實際（％） | 比較（％） |
| | 100 | 100 | 100 |
| 經費支用 | 預定(千元) | 實際(千元) | 支用率（％） |
| | 1042.6 | 1042.6 | 100 |
| 研究人員 | 計畫主持人 | 協同主持人 | 研究助理 |
| | 李憲忠 | | 莊雅婷 |
| | | | 林姿綺 |
| | | | 劉庭佑 |
| 報告頁數 | 27 | 使用語言 | 中英文並行 |
| 中英文關鍵詞 | 2018 花蓮地震、震源破裂過程 | | |
| 研究目的 | 本計畫針對台灣地區中大規模地震進行震源破裂過程的時間-空間分佈分析。所採用的方法為體波震源逆推法，透過世界地震觀測網的遠震體波資料進行快速震源逆推分析。此方法在進行分析前需要完整的震源參數資訊，包括地震規模、震源位置、震源機制、斷層面解等。目前這些資訊氣象局已於地震發生後快速地做例行公布。因此在現有的資訊架構下，於中大型地震發生後快速建立震源破裂過程的初步結果是可以達到的。此研究之目的即希望建立震源破裂之時空模擬的快速反應機制，透過計畫之執行與實際的地震案例分析來建立快速反演所需流程，並修正潛藏的系統錯誤與累積相關的研究實務經驗。 | | |
| 研究成果 | 2018 年 2 月 6 日，台灣東部花蓮地區發生規模 $M_L$ 6.1($M_w$ 6.4) 的中大型地震，造成花蓮市異常強烈的地表震動，此地震是今年於台灣本島附近第一個芮氏規模大於 6 的地震。本研究採用遠場體波、近場強地動以及 GPS 同震變形資料進行聯合逆推。結果指出，花蓮地震具有斷層跳躍破裂(fault-to-fault jumping | | |

rupture)的特性。初始破裂發生在外海的一個南北向朝西傾的斷層面，接著朝南邊的花蓮市區方向破裂。隨後，破裂跳躍到位於較淺的米崙斷層，米崙斷層破裂歷時約 10 秒，造成此次地震最大的滑移區。隨後，破裂再次跳躍到南邊的嶺頂斷層。此分析結果顯示，米崙與嶺頂斷層是由南北向朝西傾的斷層破裂所觸發，亦即米崙斷層在此次花蓮地震中是被動的。從庫倫破壞應力分析中看到，此次地震後整個花東縱谷的應力都是上升的，這個結果顯示台灣東部於將來可能仍有較高的地震危害風險。
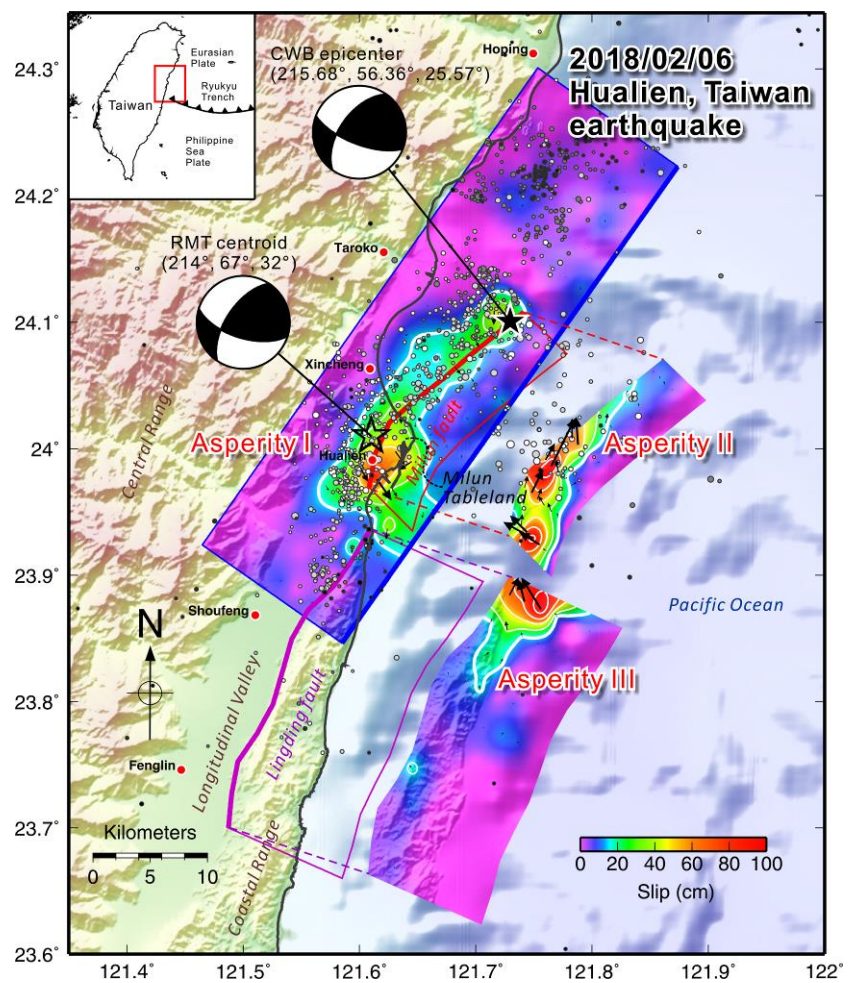


上圖為 2018 花蓮地震的錯動量分布圖。氣象局的震央位置以黑色星號表示，即時地震矩張量監測系統(RMT)所得到的 centroid 則位在震央西南邊。箭頭表示斷層面上的滑移方向與滑移量。

| | |
|---|---|
| 具體落實應用情形 | 針對 2018 花蓮地震進行快速震源破裂過程分析，可對發震區的震源破裂特性有更清楚的瞭解。逆推所建立之震源破裂模型對於後續之研究，如庫倫應力轉移分析、地震波傳遞模擬、強地動評估與都會區防災規劃等可提供重要的資訊。<br>※ 此報告之研究結果已發表在 SRL 國際期刊。 |
| 計畫變更說明 | (若有) |
| 落後原因 | (若有) |
| 檢討與建議<br>(變更或落後<br>之因應對策) | |

(以下接全文報告)

## Abstract

A fault-to-fault jumping rupture was found during the 2018 Mw 6.4 Hualien earthquake that occurred in eastern Taiwan. Joint source inversion results indicated that the initial rupture started from a north-south striking fault dipping to the west and propagated to the south with a high rupture speed. The rupture then jumped to the shallower east-dipping Milun Fault. Slip on the Milun Fault was slow and continued for more than 10 seconds, which produced the largest asperity near Hualien City. The rupture jumped again to the Lingding Fault in the northernmost Longitudinal Valley. This fault-to-fault rupture process implied that slip on Milun Fault and Lingding Fault was triggered by the N-S strike, west-dipping fault plane where the initial rupture originated. In other words, the movement on the Milun Fault was passive, it was just part of a secondary branch of the major structural system in the northernmost Longitudinal Valley. Based on this inverted source model, the static Coulomb failure stress increased along the Longitudinal Valley, which is a crucial issue for potential seismic hazards in eastern Taiwan in the near future.

## 1. Introduction

On February 6, 2018, a large earthquake struck eastern Taiwan. This earthquake had a moment magnitude of 6.4, and the epicenter (121.729°N, 24.100°E) was located in the offshore area approximately 16.5 km north of Hualien City at a depth of only 6.31 km (Figure 1). The ground shaking near the source area was extremely large, with the largest intensity being observed in Hualien City with a maximum intensity of 7 (>250 gals) based on the Central Weather Bureau (CWB) intensity scale. A high felt intensity (intensity 5, >100 gals) also extended toward the northern part of Longitudinal Valley. There were at least 17 deaths with 285 injured during this event. The strong ground

shaking caused buildings in the city of Hualien to be damaged, including four buildings that were partially collapsed and tilted. This event was the most severe earthquake to strike Hualien in the past 67 years.

More than 1000 aftershocks were detected within two week, forming a trend from northeast to southwest. The mainshock was located at the northern part of this earthquake sequence. However, the centroid location determined from the Real-time Moment Tensor monitoring system (RMT, Lee et al., 2013) was located in the south approximately 20 km away (Figure 1). This location was very close to the Milun Fault, which runs along the western edge of the Milun Tableland near Hualien City. The focal mechanisms determined from CWB and RMT all had a north-south striking, west-dipping fault. The other nodal plane was close to an E-W striking, south-dipping fault. However, there is no known active fault with a west-dipping fault plane near the source area. The only active fault is the Milun Fault, which is a strike-slip fault with a steep dipping angle toward the east (Yen et al., 2011). The field research after the earthquake observed severe surface breaks and cracks along the Milun Fault. The ruptures were mainly left lateral strike-slip, and the largest movement was more than 50 cm. Most of the damaged buildings were found along the Milun Fault (Figure 1). Apparent breaks and damage were also found on the Hualien Bridge, located across the Hualien River and close to the northern end of Lingding Fault. All of these observations indicated that the Milun Fault and/or even Lingding Fault might have been involved in the mainshock. In addition, both of the focal mechanisms (CWB and RMT) contain a strong compensated linear vector dipole (CLVD) component. The large value of CLVD also implies that the Hualien earthquake rupture could be unusual, and it might have ruptured on multi-segment fault planes or that several different fault systems were involved.

The Hualien earthquake occurred in a complex tectonic area with a high background seismicity rate. The hypocenter was located at the northern offshore of Longitudinal Valley (LV), which is a suture zone of the Eurasian Plate and Philippine Sea Plate (Tsai, 1986; Angelier et al., 1997) with a rapid convergence (Yu et al., 1997; Yen et al., 2011). The Ryukyu Trench is located on the eastern side where the Philippine Sea Plate subducted beneath the Eurasian Plate (Kao and Rau, 1999). Thousands of earthquakes occur in this junction area every year. However, the tectonic from the western end of the Ryukyu Trench to northeast offshore Taiwan is still a controversial issue. The depth of the western end of the Ryukyu Trench near the offshore of Hualien is about 40-50 km. However, the hypocenter of 2018 Hualien earthquake is at a depth of only 6.31 km. Because of the significant difference in depth, this event might be independent of the Ryukyu subduction zone.

During the time-period from October to December in 1951, three large events with magnitudes larger than $M_L$ 7 and thousands of aftershocks occurred between Hualien and Taitung along the LV. This earthquake series is known as the 1951 Hualien-Taitung

earthquake sequence (TWB, 1952; Cheng et al., 1996, 1997). The epicenter of the 2018 Hualien earthquake is very close to the one from the 1951 event (Figure 1). Due to its similarity in both magnitude and epicenter location, people are worried about the possibility of this earthquake being followed by more large events. Is it possible that this event could become the beginning of a large earthquake sequence along the LV like the 1951 events? The source model of the Hualien earthquake could be the critical clue to answer this question. In this study, we performed a joint source inversion to analyze the rupture process of the Hualien earthquake, and try to realize which faults were involved in the rupture of this event.

## 2. Data and Method

We use three data sets to perform a joint source inversion to investigate the rupture properties of the 2018 Mw 6.4 Hualien earthquake, including teleseismic body waves, local ground motion waveforms, and GPS coseismic displacements. The teleseismic data were from Incorporated Research Institutions for Seismology (IRIS). Twenty teleseismic P-wave records ranging between 30° to 90° epicentral distances were used. The records were filtered to 0.02 – 0.5 Hz passband. The local ground motion data were taken from four local seismic networks, including the CWB 24-bit Seismic Monitoring Network (CWB 24-bit), Taiwan Strong Motion Instrumentation Program (TSMIP, Kuo et al., 1995), Broadband Array in Taiwan for Seismology (BATS; Institute of Earth Sciences, 1996), and P-alert (Wu et al., 2013; 2018). We used velocity waveforms with a 60-second time window beginning from the event origin time in the inversion. The band-pass filter range of local seismic waveforms was $0.05 - 0.5$ Hz. Coseismic GPS displacements were compiled by the CWB and Institute of Earth Sciences (IES). There were 87 coseismic displacements used in the inversion.

The finite fault source inversion problem is generally formulated in a linear form, $\boldsymbol{Ax} = \boldsymbol{b}$ (Hartzell and Heaton, 1983), where $\boldsymbol{A}$ is the matrix of Green's functions, $\boldsymbol{b}$ is the observed data vector, and $\boldsymbol{x}$ is the solution vector of the slip. In this study, the inversion problem is solved by using a parallel non-negative least square (Parallel NNLS, Lee et al., 2006). A misfit function, defined as $(\boldsymbol{Ax\text{-}b})^2 / \boldsymbol{b}^2$, was used to evaluate the fit of the data. The multiple-time window method (Olson and Apsel, 1982; Hartzell and Heaton, 1983) was used, with 48-time windows each having 0.8-second duration and overlapping 0.4 seconds.

In matrix **A**, we used the IRIS Synthetics Engine (Syngine; IRIS DMC, 2015) to produce teleseismic Green's functions. A one-dimensional earth reference model that incorporates anelastic dispersion and anisotropy (anisotropic PREM; Dziewonski and Anderson, 1981) was used. For the local ground motion data, the 3D synthetic Green's functions were calculated based on the spectral-element method (SEM, Komatitsch et al., 1999; 2004; Lee et al., 2008). The local synthetic Green's functions were filtered to

the same frequency bands applied to the observed data. Geodetic Green's functions were also calculated based on three-dimensional SEM. The velocity synthetic waveforms were integrated to displacements, and then the static displacements were used to determine the geodetic Green's functions. Details of the SEM mesh model built for all of Taiwan are discussed in Lee et al., 2017.

Three fault planes were considered in this study (Figure 1). The first fault plane was based on the focal mechanism reported by the CWB. This fault plane has a N-S strike, dipping to the west (strike 215.6°, dip 56.3°, Fault 1). Since the damaged buildings and surface breaks were found along Milun Fault and Lingding Fault, we further consider these two fault planes (Fault 2 and Fault 3). The geometry and size of Fault 2 (Milun Fault) and Fault 3 (Lingding Fault) are based on the seismogenic structure source database proposed from the Taiwan Earthquake Model (TEM) project for seismic hazard analysis (Shyu et al., 2016). The three fault planes were divided into 272 subfaults, each with a size of approximately 10 km$^2$. The rupture speed was allowed to vary between 0.0 and 4.0 km/s in the inversion. Normalized weights were given for the three data sets so that the different data sets contributed equally to the inversion result. The results of the data fittings (Figures S1 to S3) are provided in the electronic supplement to this article. We had also considered the fourth fault plane in the inversion, i.e. the nodal plane of Fault 1 taken from CWB CMT that had a west to east strike, dipping to the north (strike 110.8°, dip 68.9°). Because the inverted slip amount on this nodal plane was small, we focus on the inversion results of the previous three fault planes in the following discussions.

## 3. Inversion result

**Slip complexities**

The source inversion result of the 2018 Hualien earthquake shows a complex slip pattern (Figure 2; Table S1, available in the electronic supplement to this article). Three asperities were found and each was located on a different fault plane. Asperity I was found on Fault 1 that started at the epicenter and extended to the southwest. The slip near the hypocenter was weak (approximately 40 cm). The maximum slip of this asperity was 83 cm, occurring in the southwest area approximately 20 km from the epicenter. The slip was mainly thrust with some left-lateral movement. Note that this slip concentrated area was located in the middle depths of the fault plane (8-12 km depth) just beneath Hualien City. The second slip concentrated area, the Asperity II, occurred along the shallow part of the Milun Fault plane where the surface breaks were observed. The slip was mainly left-lateral strike-slip, and the maximum movement was up to 173 cm at a depth of approximately 5.0 km. Some deep thrust slip was also found at the southern tip of Fault 2. Asperity III was located on Fault 3 close to the northern end of Lingding Fault. The slip was mainly thrust in the deeper part, and it became

left-lateral movement near the surface. The maximum slip in Asperity III was 119 cm.

The slip zone and aftershock distribution both show a northeast to southwest trend. Aftershock distribution almost filled the slip zone except for the asperity areas. Several deep aftershocks can be observed in the northern Fault 1. The other group of aftershocks was found at the eastern offshore where no fault plane exists. These aftershocks might be caused by other seismogenic structures that were induced by the mainshock.

**Fault-to-fault jumping rupture process**

The snapshots of accumulated slip are shown in Figure 3. Initial rupture presented a strong but short duration slip at the hypocenter in the first 2 seconds. This strong initial rupture also can be identified in the teleseismic P waveforms in which the P waves start from a strong short-period pulse followed by low frequency, long-period duration phases, such as ADK, TIXI, and BRVK in Figure S1. Subsequently, the rupture quickly propagated into the southwestern area. This rupture mainly occurred on Fault 1 producing a strong rupture directivity from 2 to 8 seconds. The rupture kept on slipping beneath Hualien City forming the first asperity (Asperity I). In nearly the same time period, slip also occurred on the Milun Fault (Fault 2). It ruptured slowly from 4 to 12 seconds gradually becoming Asperity II. At about the eighth second, the slip started to rupture on the Lingding fault (Fault 3). The rupture quickly occurred at the northern part of Fault 3 and slipped until about 16 seconds forming Asperity III.

Three rupture fronts with constant rupture velocities (Vr) are shown in Figure 3, they are 4.0 km/s, 3.0 km/s, and 2.0 km/s, respectively. The slip on Fault 1 occurred immediately after the Vr=3.0 km/s reference rupture front passed through. This implies that the rupture speed on Fault 1 was relatively fast. It started from the offshore area (the hypocenter) and propagated all the way toward the land (Hualien City) with a Vr of approximately 3.0 km/s. The ruptures on Fault 2 and Fault 3 were slower. Most of the slip occurred after the Vr=2.0 km/s rupture front, especially the slip on Fault 2. The lower Vr on Fault 2 indicates that the rupture of Milun Fault was more like a slow slip behavior.

The Vr 3.0 km/s on Fault 1 is a very fast rupture speed that might be close to or even greater than the shear wave speed in the shallow continental crust. However, if Fault 1 lies on the arc-continent collision boundary zone where the seismic wave speed is higher, a Vr of approximately 3.0 km/s could be a typical situation. Conversely, the rupture speeds on Fault 2 and Fault 3 are relatively slow (Vr < 2.0 km/s). This implied that Fault 2 and Fault 3 were located on the continental crust so have a slower shear wave speed. Indeed, the average shear wave speeds on Fault 1, Fault 2, and Fault 3, determined from a tomography model (Huang et al., 2014), are 3.14, 2.84, and 2.62 km/s, respectively.

A complex seismic moment release history can be found from the moment rate function

(Figure 4). A short period peak occurred during the first 1-2 seconds, which was caused by a strong initial rupture near the hypocenter. From 2 to 10 seconds, a significant amount of moment release showing a peak at about $7^{th}$ second. This moment release is related to the developments of Asperity I and Asperity II. The other time-period moment release is between 10 and 15 seconds, which was related to the rupture of Asperity III. The entire duration time of Hualien earthquake is about 17 seconds, with three peaks during the $1^{st}$, $7^{th}$, and $11^{th}$ seconds. The total seismic moment is about $9.4 \times 10^{18}$ Nm, which is equivalent to a Mw 6.58 earthquake.


## 4. Discussion

For the local ground motion data, we found the synthetic waveforms for the stations near the Milun Tableland and the estuary of the Hualien River poorly fit the observed horizontal components, such as HWA058, HWA060 (Figure S3). The phases and arrival times are comparable, but the maximum amplitudes are underestimated. This could be due to a strong site effect or a non-linear effect caused by thick sedimentary deposits. To confirm the reliability of the source model, we calculated the permanent surface displacement based on SEM and compared it with the InSAR coseismic deformation data (Figure 5). In general, the synthetic permanent displacement is comparable with the InSAR surface deformation. The Milun Tableland was characterized by obvious uplift and moved to the east. Conversely, the western side of Milun Fault mainly moved toward the west. The InSAR deformation pattern shows different characteristics at the two sides of the northern Lingding Fault. This phenomenon can also be reconstructed by the synthetic surface deformation. Both the observed and synthetic vertical components showed uplift across most of the northernmost LV. However, some subsidence can be found in the InSAR data near Hualien City. This second-order characteristic was not able to completely describe by the synthetic surface deformation.

We analyzed the contribution from each fault in the local ground motion and GPS data. For the local ground motion data, three stations near Fault 1, Fault 2 and Fault 3 were selected (Figure S4, available in the electronic supplement to this article). Results indicated that the characteristic of local waveforms was controlled by the vicinity fault. The contribution of Fault 1 was mainly at the beginning of ground shaking recorded by NACB station. The slip of Fault 2 and Fault 3 dominated the characteristic of largest phase in HWA023 and W00D, respectively. The surface coseismic movement also shows a similar result in which the GPS data was very sensitive to the inverted source model. Due to poor data quality in the vertical component, we only analyzed the result in horizontal. The data fit poorly when considered individual slip on Fault 1, Fault 2 or Fault 3 (Figure S5, available in the electronic supplement to this article). Only the complete slip pattern of all three faults showed a better fit to the observed GPS data.

The rupture of the 2018 Hualien earthquake occurred on at least three fault systems, the

Milun Fault, Lingding Fault, and the N-S strike west-dipping fault. The first two faults are known active faults reported by the Central Geological Survey (Chang et al., 1998). The third one, however, had never been identified in previous studies. Shyu et al. (2016) proposed a structural development model for the northernmost LV. In their model, the Coastal Range subducted northward beneath the Eurasian Plate together with the Philippine Sea Plate. Since the N-S striking fault was dipping to the west and down to about a 15-20 km depth, it is very possible for it to be formed between the Coastal Range and Central Range bedrocks. The other possibility is that the fault is the boundary fault between Coastal Range bedrock and shallow LV sediments because the main slip area on Fault 1 was at a depth of approximately 10 km.

Shyu et al., (2016) relocated seismicity in eastern Taiwan and indicated that no earthquakes are present directly below the Milun Tableland, suggesting that the Milun Fault has not been seismically active during the past 20 years. This inference is consistent with the source model of this event. The rupture started from the middle depths of the N-S strike, west-dipping fault, then jumped to the Milun Fault, which caused the surface rupture. This implied that the movement on the Milun Fault was passive, and it was just part of a secondary branch of the major structural system. Figure 6 provides this conceptual tectonic model for the northernmost LV inferred from the 2018 Hualien earthquake. The Coastal Range bedrock is subducting northward beneath the Eurasian plate together with the Philippine Sea plate. The N-S striking, west-dipping fault is the boundary fault between the Coastal Range and Central Range and/or the boundary between the Coastal Range bedrock and shallow LV sediments. This western dipping fault could be the northern extension of the Central Range fault. The Milun Fault, which is located at shallower depths and dipping toward the east, is just part of a secondary branch of this major structural system, i.e. the deeper N-S strike, west-dipping fault in northernmost LV. According to the TEM seismogenic structure model, the geometry of Fault 3 is defined as an east-dipping thrust fault with some left lateral movement. However, in this conceptual tectonic model (Figure 6), the southern extension of Fault 1 could be connected to the surface trace of Fault 3. If Fault 1 and Fault 3 belong to the same fault system, which is the boundary fault between Coastal Range bedrock and shallow LV sediments, both of these two faults might be dipping to the west.

Finally, we calculated the static Coulomb failure stress change (ΔCFS) along LV using the source model determined from the joint source inversion. Two different receiver fault plane mechanisms at depths 15 km were considered. One is the N-S striking, east-dipping fault (strike 215°, dip 56°, rake 25°) that is close to the geometry of the Central Range Fault discussed above. The other is the Lingding Fault (strike 25°, dip 60°, rake 45°), which is close to the mechanism of the east-dipping Longitudinal Valley Fault. Results show that the ΔCFS caused by the Hualien earthquake was complex in the source area. The aftershocks occurred in both regions, where ΔCFS increased and decreased (Figure 7). These results again point out that the Hualien earthquake

mainshock and its aftershocks occurred on a complex tectonic region where several active seismogenic structures are involved. In addition, because the background seismicity rate is fairly high in this region, the aftershocks could occur in all areas of the stress field (Kanamori and Brodsky, 2004). Note that the $\Delta$CFS appeared to increase along the LV due to mechanisms from either the Longitudinal Valley Fault or the Central Range Fault.

## 5. Conclusion

Joint inversion results show that the source of the Hualien earthquake was complex and contains three asperities on different fault systems. The slip started from an N-S striking, west-dipping fault at about 6-10 km depth with a high rupture speed of approximately 3.0 km/s. Then, the rupture jumped to the Milun Fault and Lingding Fault. This fault-to-fault rupture process implied that the slip on the Milun Fault and Lingding Fault could be triggered by the N-S strike, west-dipping fault where the initial rupture originated. In other words, the movement on the Milun Fault was passive; it is just part of a secondary branch of the major structural system in northernmost LV. The 1951 $M_L7.3$ Hualien event could also have occurred in the same way in which the initial slip started on an offshore seismogenic structure and then triggered the rupture along the Milun Fault.

Results also point out that the static Coulomb failure stress change has apparently increased along the LV. Previous studies indicate that the static Coulomb stress change alone cannot explain the time lag between the main event and triggered events (Chen et al., 2008). However, it is not possible to conclude that eastern Taiwan is free from large earthquakes after the 2018 Hualien earthquake.

## Data and Resources

P-alert waveform data are available at http://palert.earth.sinica.edu.tw/db/ (last accessed June 2018). The CWB 24-bit data was taken from the Taiwan rapid earthquake information release system implemented by the Central Weather Bureau at http://gdms.cwb.gov.tw (last accessed June 2018).

## Acknowledgements

# References

Angelier, J., H. T. Chu, and J. C. Lee (1997). Shear concentration in a collision zone: kinematics of the Chihshang Fault as revealed by outcrop-scale quantification of active faulting, Longitudinal Valley, eastern Taiwan, *Tectonophysics* **274** 117-143.

Chang, H. C., C. W. Lin, M. M. Chen, and S. T. Lu (1998). An Introduction to the Active Faults of Taiwan: Explanatory Text of the Active Fault Map of Taiwan. Scale 1:500,000. *Spec. Publ. of Cent. Geol. Surv. Taiwan*, 10, 103.

Chen, K. H., S. Toda, and R. J. Rau (2008). A leaping, triggered sequence along a segmented fault: the 1951 Hualien – Taitung earthquake sequence in eastern Taiwan, *J. Geophys. Res.* **113** B02304, doi:10.1029/2007JB005048.

Cheng, S. N., T. T. Yu, Y. T. Yeh, Z. S. Chang (1997). Relocation of the 1951 Hualien, Taitung earthquake sequence, conference on weather analysis and forecasting, Proceedings of Marine Meteorology and Seismology, in Commemoration of 100 Years of Weather Observation in the Taiwan Area, 690–699.

Cheng, S. N., Y. T. Yeh, M. S. Yu (1996). The 1951 Taitung earthquake in Taiwan, *J. Geol. Soc. China* **39** 267–285.

Dziewonski, A. M. and D. L. Anderson (1981). Preliminary reference Earth model (PDF), *Physics of the Earth and Planetary Interiors*, **25**(4) 297–356.

Hartzell, S. H., and T. H. Heaton (1983). Inversion of strong ground motion and teleseismic waveform data for the fault rupture history of the 1979 Imperial Valley, California earthquake, *Bulletin of the Seismological Society of America* **73** 1553–1583.

Institute of Earth Sciences, Academia Sinica, Taiwan (1996). Broadband Array in Taiwan for Seismology. Institute of Earth Sciences, Academia Sinica, Taiwan. Other/Seismic Network. doi:10.7914/SN/TW

IRIS DMC (2015). Data Services Products: Synthetics Engine, https://doi.org/10.17611/DP/SYNGINE.1.

Kanamori H., and E. E. Brodsky (2004). The physics of earthquake, *Rep. Prog. Phys.* **67** 1429

Kao, H., and R. J. Rau (1999). Detailed structures of the subducted Philippine Sea plate beneath northeast Taiwan: a new type of double seismic zone, *J. geophys. Res.* **104** 1015–1033.

Komatitsch, D., and J. Tromp (1999). Introduction to the spectral-element method for 3-D seismic wave propagation, *Geophysical Journal International* **139** 806-822.

Komatitsch, D., Q. Liu, Q., J. Tromp, P. Süss, C. Stidham, and J. H. Shaw (2004). Simulations of ground motion in the Los Angeles basin based upon the spectral-element method, *Bull. Seismol. Soc. Am.* **94** 187–206.

Kuo, K. W., T. C., Shin, and K. L. Wen (1995). Taiwan strong motion instrumentation program (TSMIP) and preliminary analysis of site effects in Taipei basin from strong motion data, in Urban Disaster Mitigation: The Role of Engineering and Technology, Edited by F. Y. Cheng and M.-S. Sheu, Elsevier Science, 47-62.

Lee, S. J. (2017). Lessons Learned from Source Rupture to Strong Ground Motion Simulations: An Example from Taiwan, *Bulletin of the Seismological Society of America* **107** 2106-2116, doi:10.1785/0120170030.

Lee, S. J., H. W. Chen, Q. Liu, D. Komatitsch, B. S. Huang, and J. Tromp (2008). Three dimensional simulations of seismic wave propagation in the Taipei basin with realistic topography based upon the spectral-element method, *Bull. Seismol. Soc. Am.* **98** 253–264. http://dx.doi.org/10.1785/0120070033.

Lee, S. J., K. F. Ma, H. W. Chen (2006). Three-dimensional dense strong motion waveform inversion for the rupture process of the 1999 Chi-Chi, Taiwan, earthquake, *J. Geophys. Res.: Solid Earth* (1978–2012) **111**, B11.

Lee, S. J., W. T. Liang, H. W. Cheng, F. S. Tu, K. F. Ma, H. Tsuruoka, H. Kawakatsua, B. S. Huang, and C. C. Liu (2013). Toward real-time regional earthquake simulation I: real-time moment tensor monitoring (RMT) for regional events in Taiwan, *Geophys. J. Int.* **87** 56-68.

Olson, A. H., and R. J. Apsel (1982). Finite faults and inverse theory with applications to the 1979 Imperial Valley earthquake, *Bull. seism. Soc. Am.* **72** 6A 1969-2001.

Shyu, J. B. H., Y. R. Chuang, Y. L. Chen, Y. R. Lee, and C. T. Cheng (2016). A new on-land seismogenic structure source database from the Taiwan Earthquake Model (TEM) project for seismic hazard analysis of Taiwan, *Terr. Atmos. Ocean. Sci.* **27** 311-323, doi: 10.3319/ TAO.2015.11.27.02(TEM).

Shyu J. B. H., C. F. Chen, Y. M. Wu (2016). Seismotectonic characteristics of the northernmost Longitudinal Valley, eastern Taiwan：Structural development of a vanishing suture, *Tectonophysics*, 692, 295-308.

Tsai, Y. B. (1986). Seismotectonics of Taiwan, *Tectonophysics* **125** 17–38.

TWB (1952). The 1951 Earthquake Report, Taiwan Weather Bureau, Taipei. 83pp

Wu, Y. M., D. Y. Chen, T. L. Lin, C. Y. Hsieh, T. L. Chin, W. Y. Chang, W. S. Li, and S. H. Ker (2013). A high-density seismic network for earthquake early warning in Taiwan based on low cost sensors, *Seismol. Res. Lett.* **84**(6) 1048–1054.

Wu, Y. M., H. Mittal, T. C. Huang, B. M. Yang, J. C. Jan, and S. K. Chen (2018). Performance of a Low-Cost Earthquake Early Warning System (P-Alert) and shake map production during the 2018 Mw 6.4 Hualien (Taiwan) Earthquake. (in this issue)

Yen, J. Y., C. H. Lu, C. P. Chang, A. J. Hooper, Y. H. Chang, W. T. Liang, T. Y. Chang, M. S. Lin, and K. S. Chen (2011). Investigating active deformation in the northern Longitudinal Valley and City of Hualien in eastern Taiwan using persistent scatterer and small-baseline SAR interferometry, *Terr. Atmos. Ocean. Sci.* **22**(3) 291-304, doi: 10.3319/TAO.2010.10.25.01(TT)

Yu, S. B., H. Y. Chen, and L. C. Kuo (1997). Velocity field of GPS stations in the Taiwan area, *Tectonophysics* **274** 41-59.
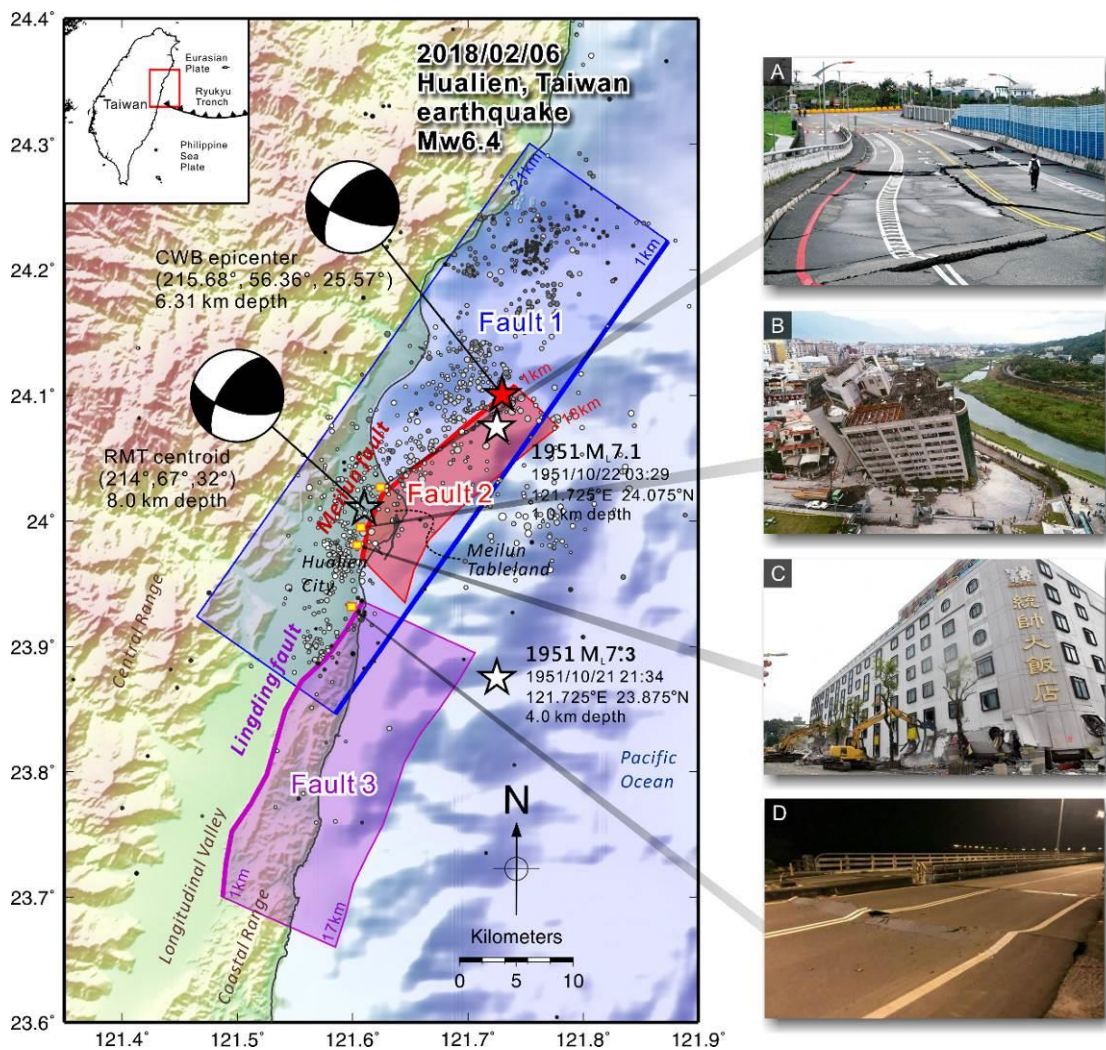
**Figure 1.** The 2018 Mw 6.4 Hualien earthquake in eastern Taiwan. The CWB epicenter is indicated with a red star and the RMT centroid location is shown as an open star. The white stars are two $M_L > 7$ events of the 1951 Hualien-Taitung earthquake sequence. Beach balls show the focal mechanisms determined by the CWB CMT and RMT. Gray color circles are the aftershocks occurred within two week. The three fault planes considered in this study are projected to the surface and shown by blue, red and purple colors, respectively. Right photos show the damaged buildings caused by Hualien earthquake: (A) Malongayangay Bridge, (B) Yun Men Tsui Ti building, (C) Marshal Hotel, and (D) Hualien Bridge.
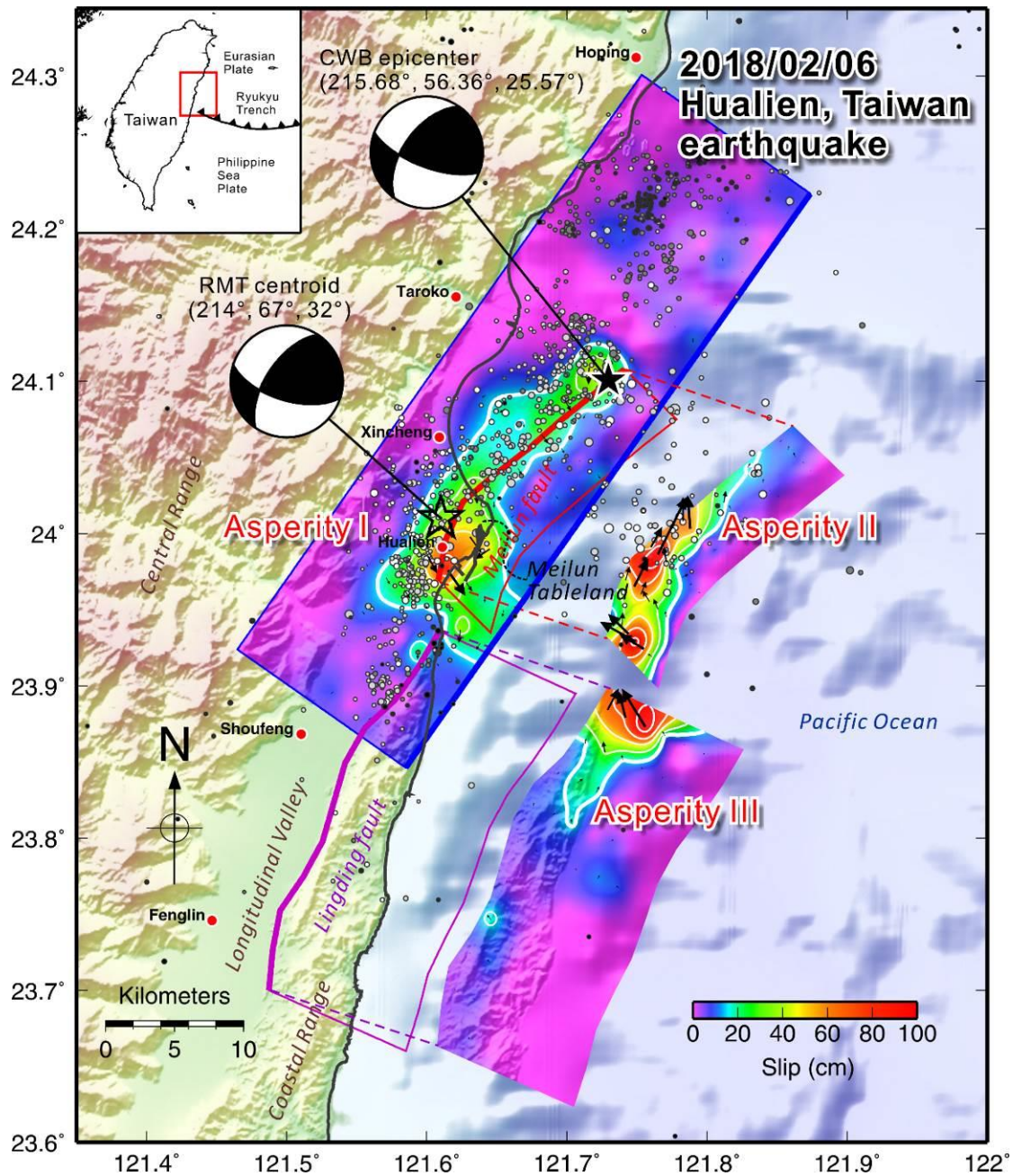
**Figure 2.** Slip distribution of the joint source inversion result. The CWB epicenter is indicated with a solid black star and the RMT centroid location is shown as an open star. Beach balls show the focal mechanisms determined by the CWB CMT and RMT. Gray color circles are the aftershocks occurred within two week.
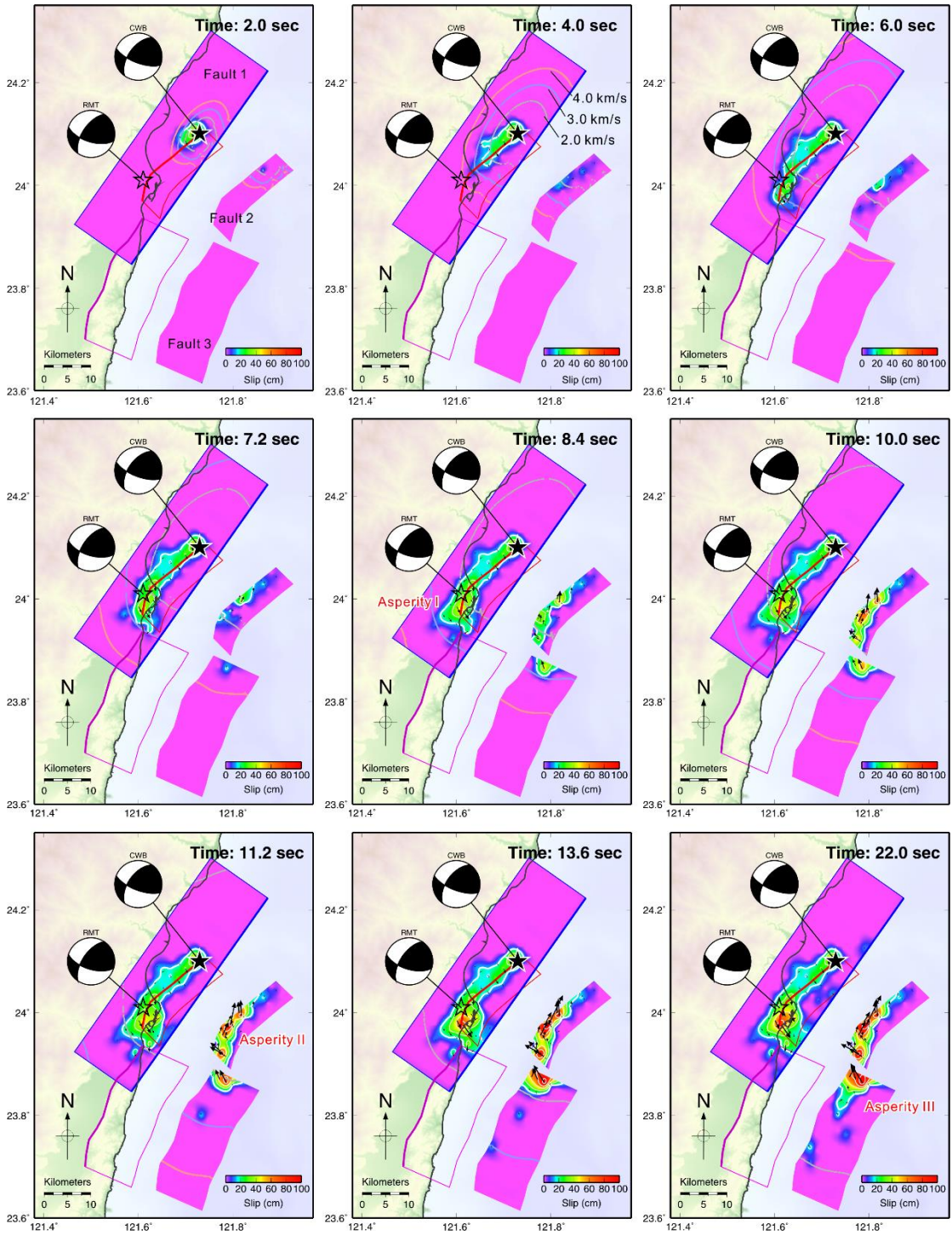
**Figure 3.** Rupture snapshots of cumulative slip. The star shows the epicenter reported by CWB. Vectors are the slip direction and the amount of cumulative slip on each subfault. The light-color curved lines indicate three reference rupture fronts with Vr = 2.0 km/s, Vr = 3.0 km/s and Vr = 4.0 km/s, respectively.

16
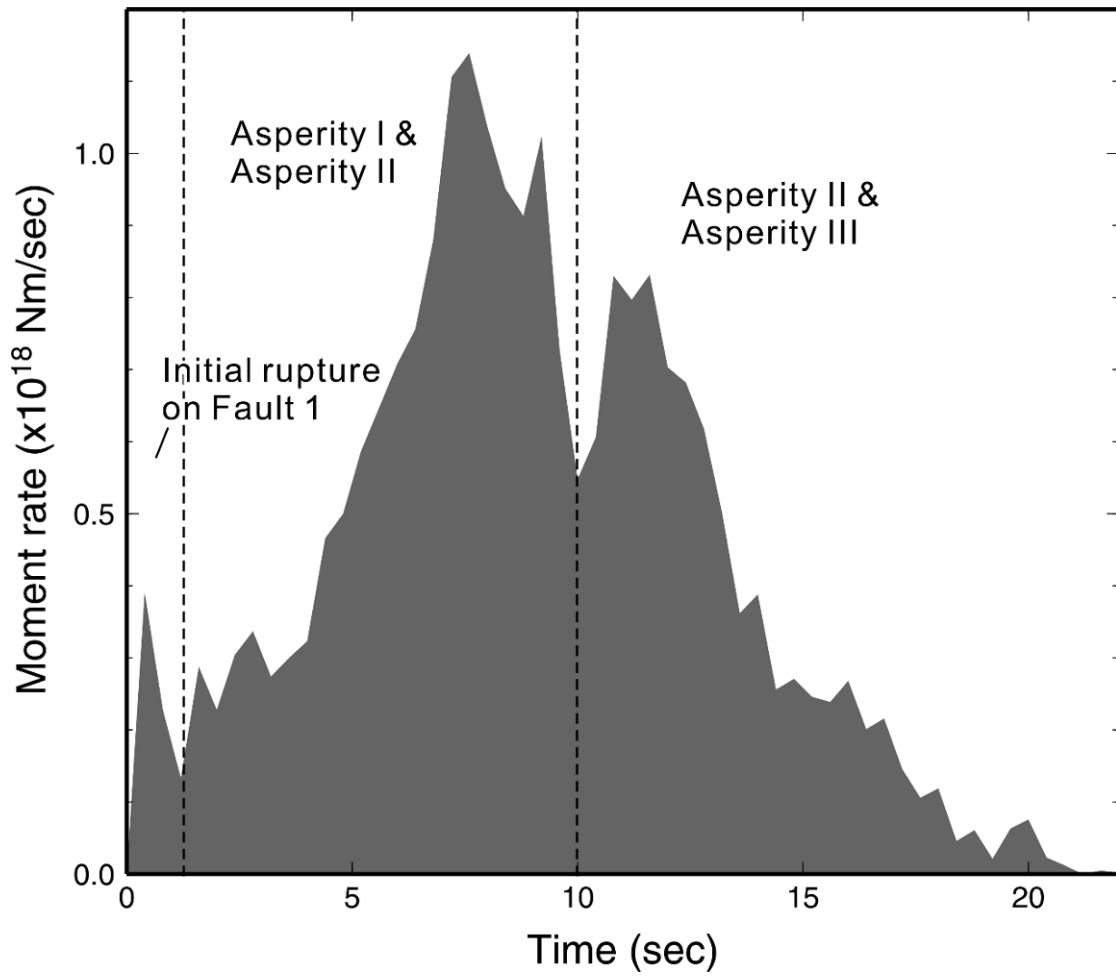
**Figure 4.** Moment rate function of the 2018 Hualien earthquake. Three time periods of associated energy releases are delineated by dashed lines. The total seismic moment is about $9.4 \times 10^{18}$ Nm, which is equivalent to a Mw 6.58 earthquake.
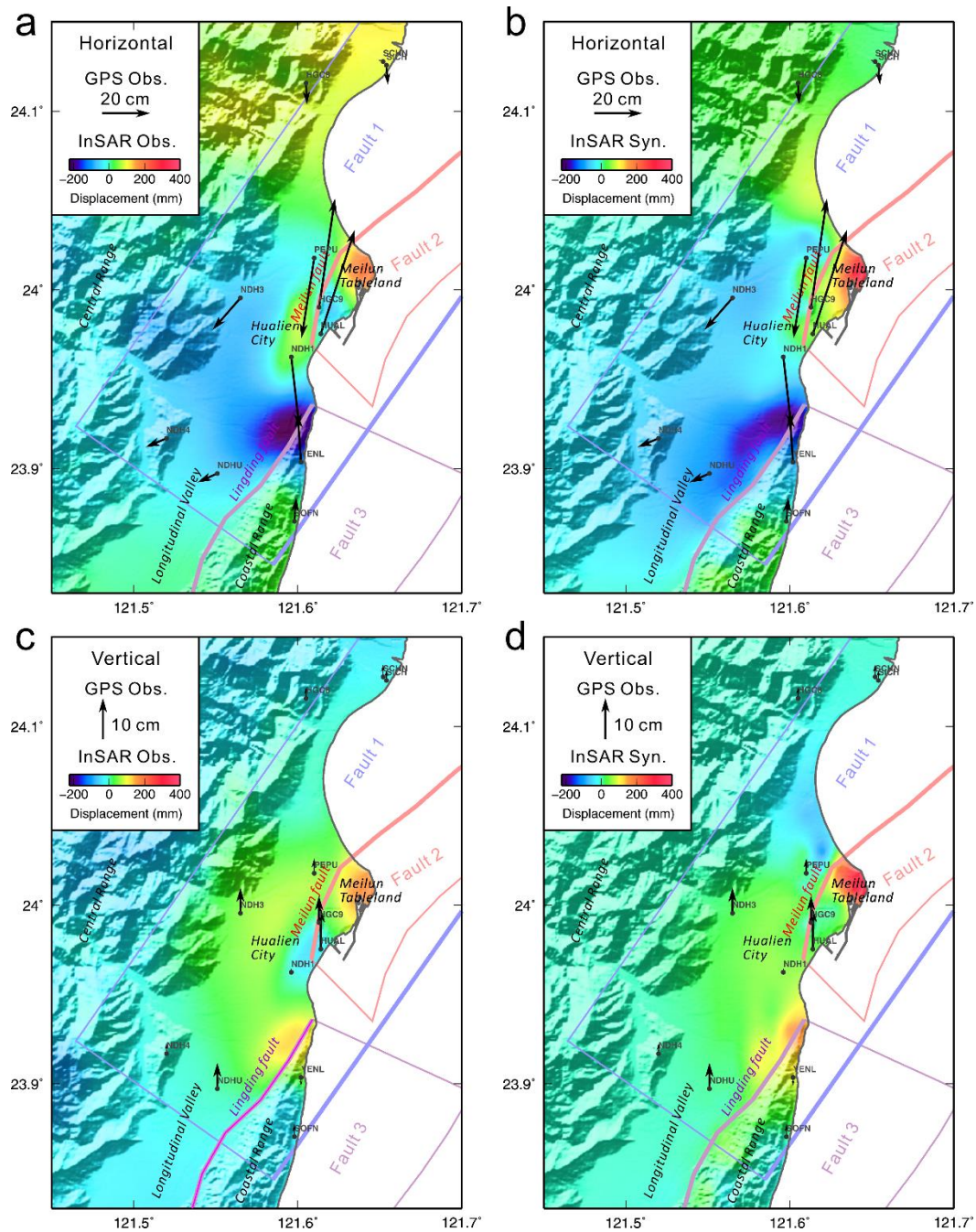
**Figure 5.** Comparison of observed InSAR coseismic deformation pattern and synthetic permanent surface displacement. (a) Observed InSAR deformation pattern in horizontal (E-W) component, (b) Synthetic permanent surface displacement in horizontal (E-W) component, (c) Observed InSAR deformation pattern in vertical (U-D) component, (d) Synthetic permanent surface displacement in vertical (U-D) component. The GPS coseismic displacements are also shown in these results for comparison.
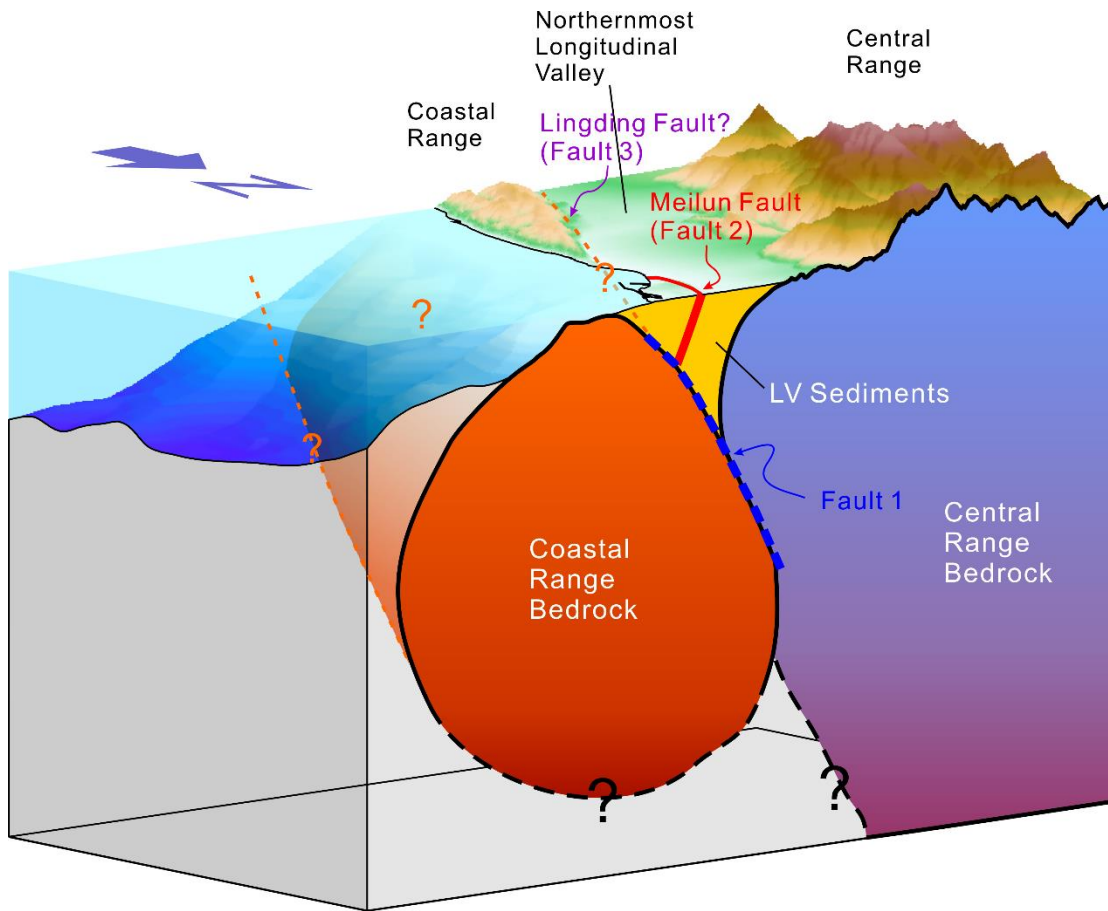
**Figure 6.** Conceptual tectonic model for the northernmost LV inferred from the 2018 Hualien earthquake. Blue dotted line shows the N-S striking, west-dipping fault which is the boundary fault between the Coastal Range and Central Range and/or the boundary between the Coastal Range bedrock and shallow LV sediments. This western dipping fault could be the northern extension of the Central Range fault. The red line indicates the Meilun Fault, which is located at shallower depths and dipping toward the east. It is part of a secondary branch of this major structural system, i.e. the deeper N-S strike, west-dipping fault in northernmost LV.
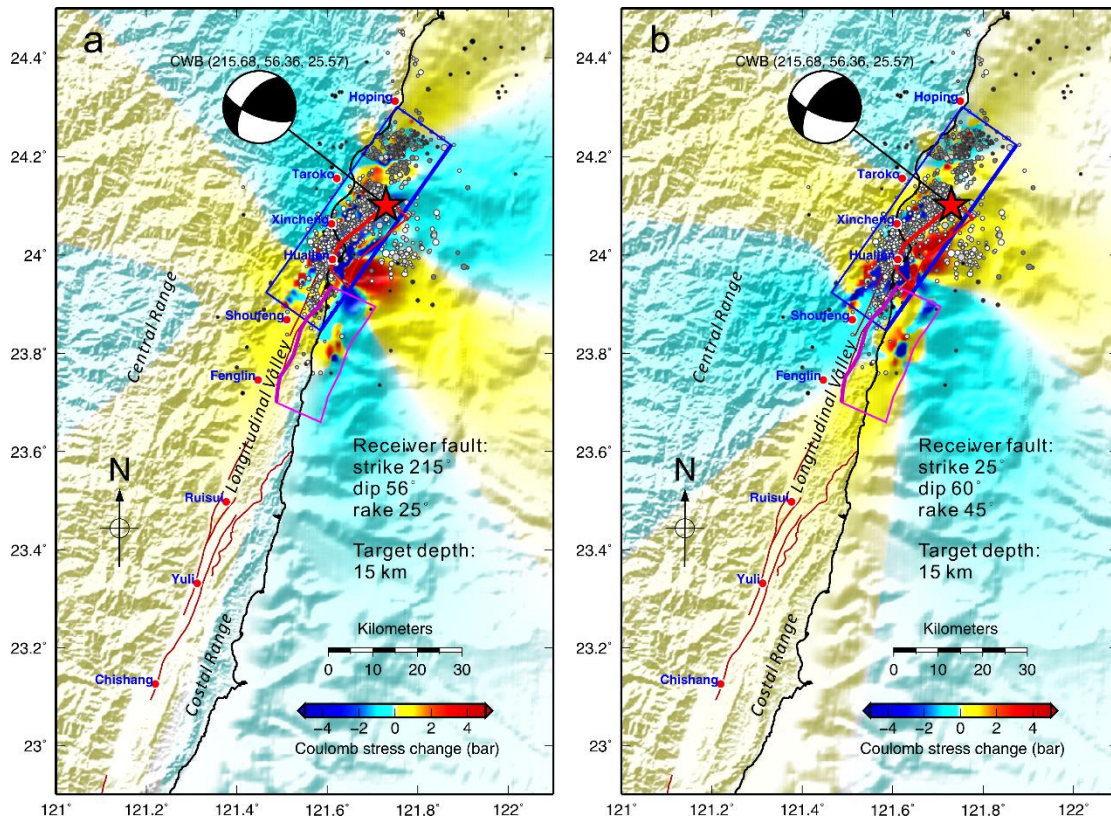
**Figure 7.** The result of Coulomb stress changes caused by the inverted finite-fault source model. The three fault planes used in this study are projected to the surface and shown with blue, red and purple colors, respectively. The CWB epicenter is indicated with a red star. Two different receiver fault plane mechanisms at depths 15 km were considered: (a) the N-S striking, east-dipping fault (strike 215°, dip 56°, rake 25°) that is close to the geometry of the Central Range Fault, (b) the Lingding Fault (strike 25°, dip 60°, rake 45°), which is close to the mechanism of the east-dipping Longitudinal Valley Fault.

Electronic Supplement to

**Fault-to-fault jumping rupture of the 2018 Mw 6.4 Hualien earthquake in eastern Taiwan**

by Shiann-Jong Lee, Tzu-Chi Lin, Ting-Yu Liu and Tong-Pong Wong

This electronic supplement includes five figures that show the data fittings of the inversion result.
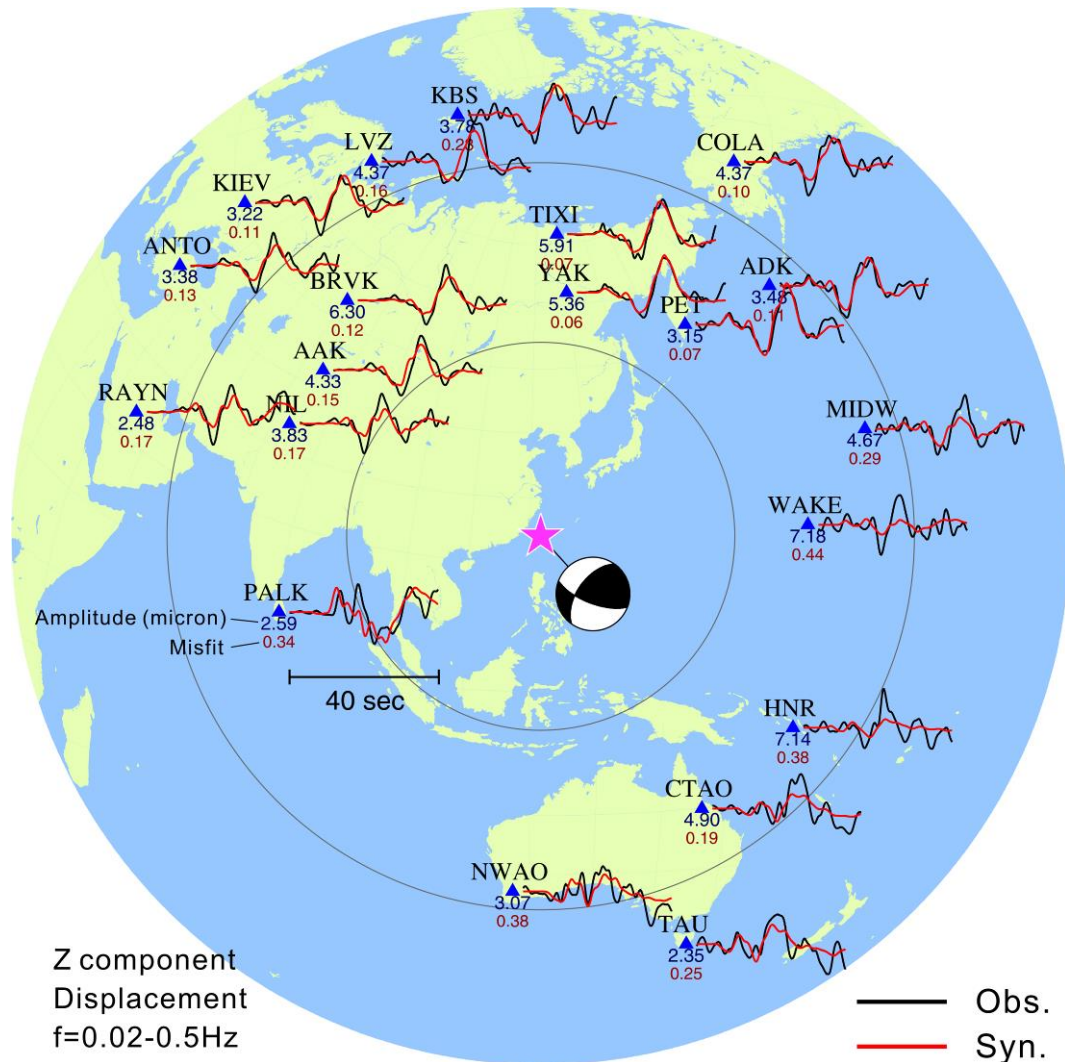
**Figure S1.** Comparisons between observed teleseismic P waves and synthetic waveforms. Black and red lines are the observed and synthetic waveforms, respectively. The pink star shows the epicenter of 2018 Hualien earthquake and the beach ball indicates the focal mechanism determined by the CWB. All the waveforms are displacement-type and a band-pass filter of 0.02 to 0.5 Hz is employed. The maximum observed displacement and waveform misfit are shown at each station. The waveform misfit of teleseismic data was 0.38.
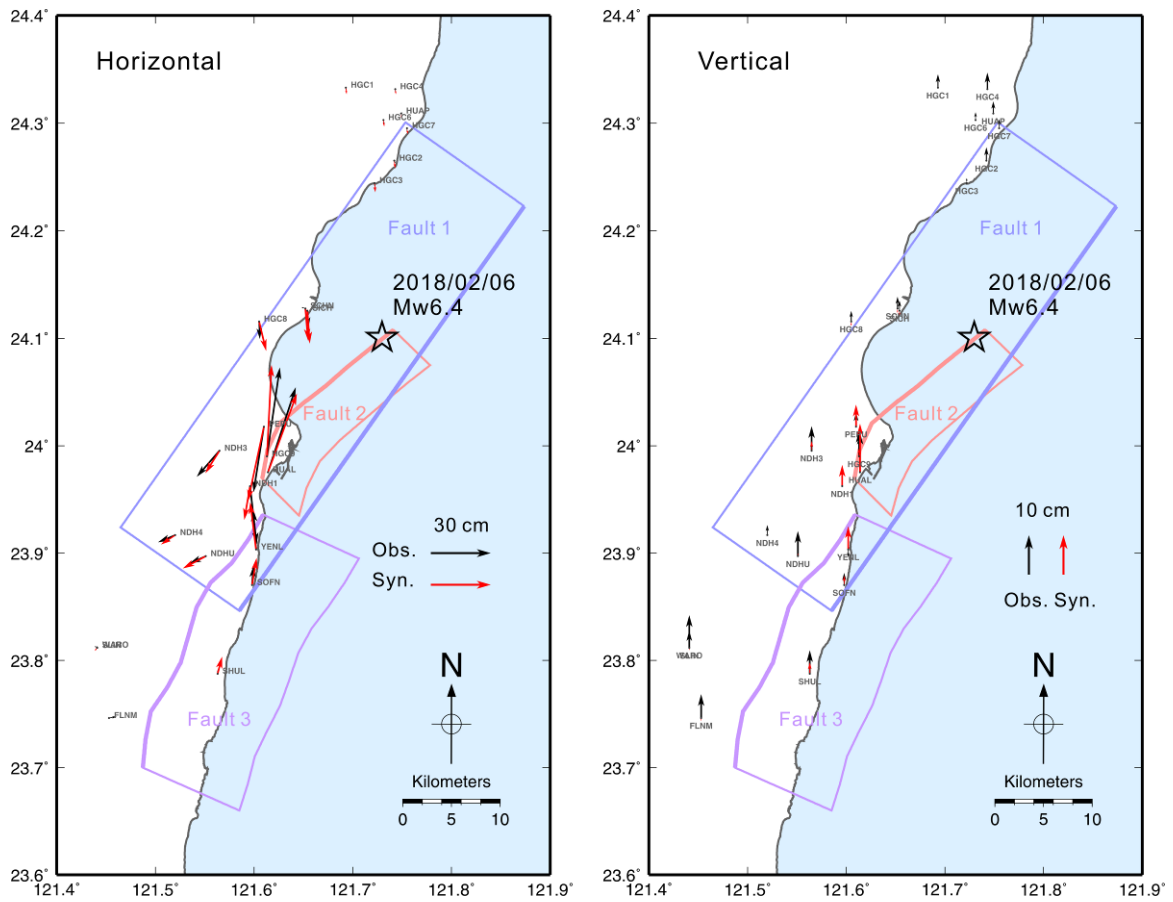
**Figure S2.** Comparison between observed GPS coseismic displacements and synthetic surface deformation. The left panel shows the coseismic displacements in horizontal component and right panel is the vertical component. Black and red arrows are the observed and synthetic displacements, respectively. The open star indicates the epicenter. The three fault planes considered in this study are projected to the surface and shown by blue, red and purple colors, respectively. Misfit of GPS data was 0.22.
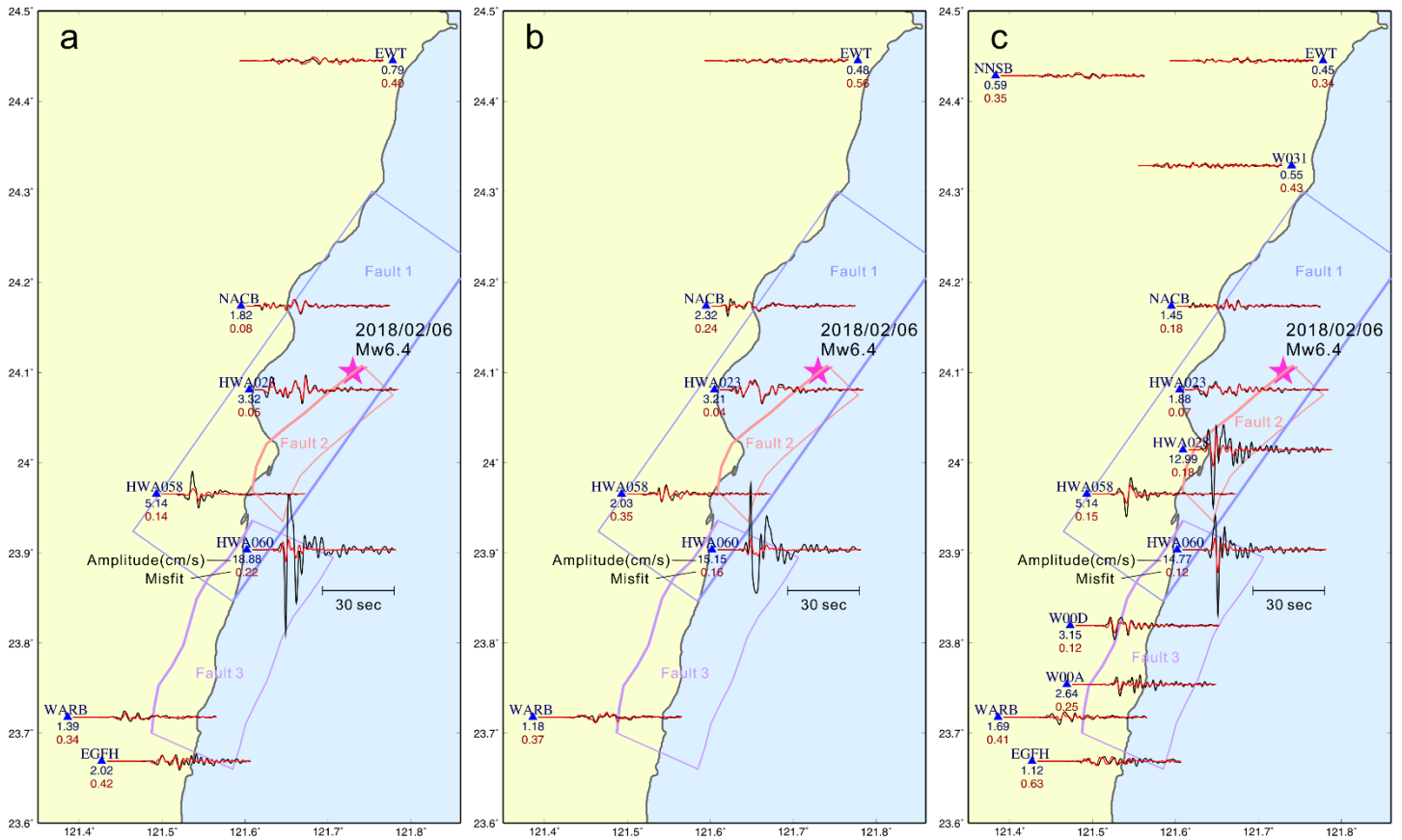
**Figure S3.** Comparisons between observed and synthetic local ground motion waveforms. From left to right are (a) east-west component, (b) north-south component, and (c) vertical component. Black and red lines are the observed and synthetic waveforms, respectively. The pink star shows the epicenter. All the waveforms are velocity-type and a band-pass filter of 0.05 to 0.5 Hz is employed. The maximum observed ground velocity and waveform misfit are shown at each station. The misfit of local ground motion waveform was 0.43.
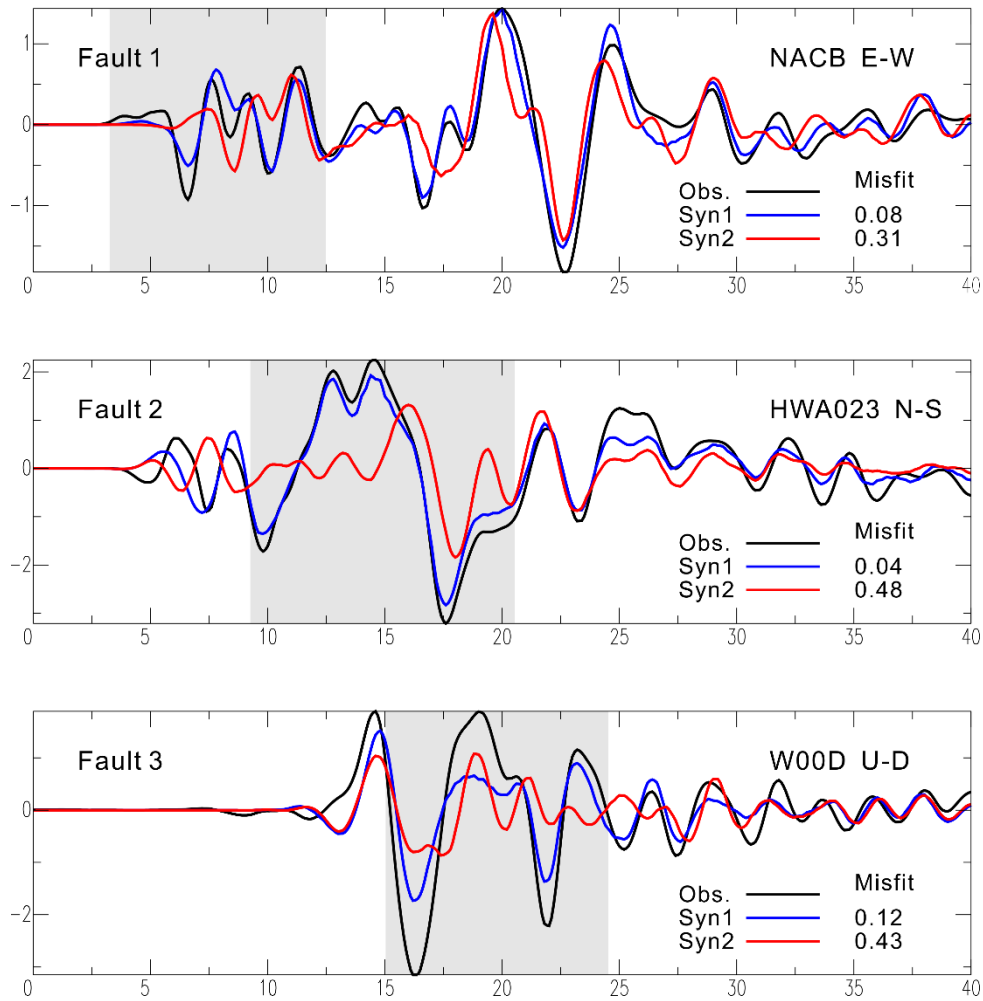
**Figure S4.** Contribution from each fault in the local ground motion data. Three local stations near Fault 1, Fault 2 and Fault 3 are analyzed. From up to down are (a) Fault 1, NACB in E-W component, (b) Fault 2, HWA023 in N-S component and (c) Fault 3, W00D in vertical component. Black, blue and red lines are observed data, synthetic waveform determined from all three faults and synthetic waveform without the target fault, respectively. All the waveforms are velocity-type and a band-pass filter of 0.05 to 0.5 Hz is employed. The gray color background marks the main contribution of the target fault in the seismogram. The waveform misfit is shown at the lower right.
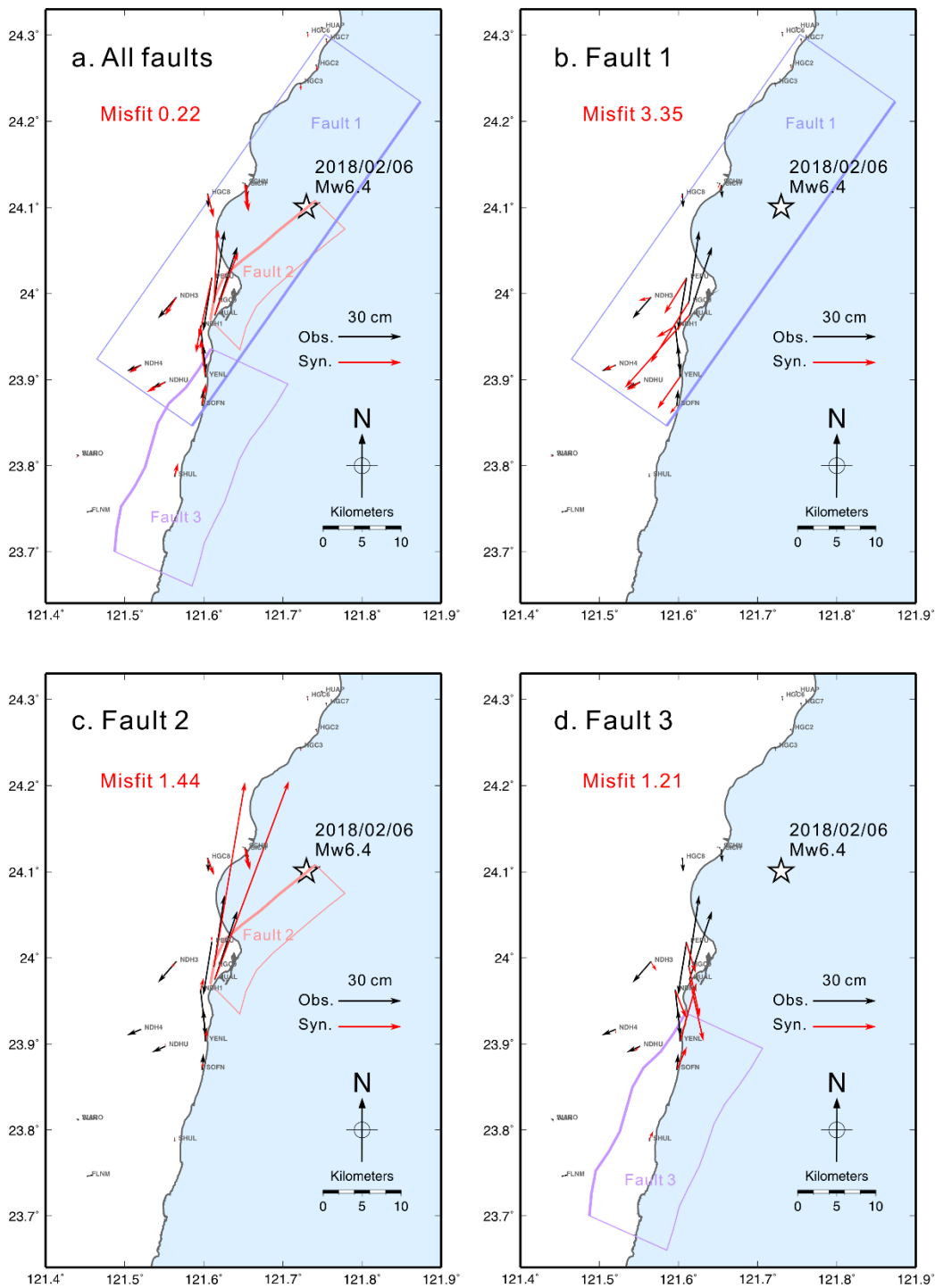
**Figure S5.** Comparison between observed GPS coseismic displacements and synthetic surface deformation determined from (a) all three fault planes, (b) only Fault 1, (c) only Fault 2, and (d) only Fault 3. Black and red arrows are the observed and synthetic displacements, respectively. The fault plane considered in each case is projected to the surface. Misfit of GPS data is shown at upper left.

# 【附件】赴大陸地區出差或研習心得報告

| 姓名 | 林姿綺 | | |
|---|---|---|---|
| 服務單位及職位 | 國立台灣大學地質科學學系暨研究所 博士班 | | |
| 活動日期 | 2018 年 5 月 7 日至 6 月 2 日 | 地點 | 中國安徽省合肥市 中國科學技術大學 |
| 出國類別 | 教育進修 | | |

**心 得**

　　2018 年 2 月 6 日，台灣東部發生 Mw6.4 的地震。震央(121.729°N，24.100°E)位於距離花蓮市約 20 公里的海域，其深度只有 6.31 公里。震央附近的地面震動非常大，花蓮市最大震度達到 7 級，造成四座建築物部分倒塌傾斜，並至少有 17 人死亡，285 人受傷。此為 67 年來發生的最嚴重的地震。此外，由中央氣象局和中研院李憲中博士之即時地震矩張量監測系統解算的震源機制解，都包含強補償線性向量偶極(Compensated-Linear-Vector-Dipole, CLVD)分量。此種大的 CLVD 數值結果，意味著花蓮地震的破裂是較複雜的，破裂可能發生在多段斷層面或多個不同的斷層系統中。

　　現今台灣對於震源破裂的探討方式，普遍皆以運動學角度進行分析，當中 包含斷層破裂時間和錯動量等，較少以震源破裂動力學的角度討論斷層自發性破裂的過程。但對於複雜斷層系統，若可以藉由動力學的角度探討破裂過程，可以幫助我們得到基於物理性質的破裂起始、傳播和終止模型。若以震源動力學的觀點來切入問題，需要對斷層面上的物理特性，如正應力、初始應力分布、摩擦係數、震後可能的應力降等參數進行假設與分析，進而讓破裂過程自發性的產生與終止。本人於博士班期間多次赴中國安徽省合肥市中國科學技術大學之地球與空間科學學院訪問，此為第四次至中國科學技術大學訪問，為期約一個月。此次訪問主要與中國科學技術大學地球與空間科學學院之副研究員-胡峰和陳曉非院士團隊學習計算震源破裂動力學的方法。基於前幾次訪問時，習得之動力學標準模型，應用至 2018 年 2 月 6 日的花蓮地震。以動力學震源破裂模型可用更客觀的方式探討此地震的發生、破裂過程，同時因此次地震斷層系統可能較為複雜，可以透過此物理模型來探討破裂過程中，應力是否會由較深的斷層跳躍至較淺的米崙斷層，進而引發地表破裂，因此造成當時花蓮市區的房屋倒塌。本研究最終目的希望藉由此次地震事件的研究經驗，未來也可應用至潛在可能發生破裂的斷層系統，提供研擬防災對策的重要參考。

　　此趟特別感謝中國科學技術大學-地球與空間科學學院之孫道遠教授以及楊欣穎特聘副研究員，在此次訪問中給予我許多生活以及學術上的幫助。也感謝合作者胡峰副研究員和陳曉非院士，授予我許多動力學相關知識並提供我在當地的辦公空間。